OPEN ACCESS



Confirmation of Color-dependent Centroid Shift Measured After 1.8 Years with HST

Aparna Bhattacharya^{1,2}, David P. Bennett^{1,2}, Jean Philippe Beaulieu^{3,4}, Ian A. Bond⁵, Naoki Koshimoto^{6,7}, Jessica R. Lu⁸, Joshua W. Blackman⁴, Clément Ranc³, Aikaterini Vandorou^{1,2}, Sean K. Terry⁸, Jean Baptiste Marquette³, Andrew A. Cole⁴, and Akihiko Fukui^{9,10}

Code 667, NASA Goddard Space Flight Center, Greenbelt, MD 20771, USA; abhatta5@umd.edu
 Department of Astronomy, University of Maryland, College Park, MD 20742, USA
 UPMC-CNRS, UMR 7095, Institut d'Astrophysique de Paris, 98Bis Boulevard Arago, F-75014 Paris, France
 School of Physical Sciences, University of Tasmania, Private Bag 37 Hobart, Tasmania 7001 Australia
 Institute of Natural and Mathematical Sciences, Massey University, Auckland 0745, New Zealand
 Department of Astronomy, The University of Tokyo, 7-3-1 Hongo, Bunkyo-ku, Tokyo 113-0033, Japan
 National Astronomical Observatory of Japan, 2-21-1 Osawa, Mitaka, Tokyo 181-8588, Japan
 University of California Berkeley, Berkeley, CA, USA

Abstract

We measured the precise masses of the host and planet in the OGLE-2003-BLG-235 system, when the lens and source were resolving, with 2018 Keck high resolution images. This measurement is in agreement with the observation taken in 2005 with the Hubble Space Telescope (HST). In the 2005 data, the lens and sources were not resolved and the measurement was made using color-dependent centroid shift only. The Nancy Grace Roman Space Telescope will measure masses using data typically taken within 3–4 yr of the peak of the event, which is a much shorter baseline when compared to most of the mass measurements to date. Hence, the color-dependent centroid shift will be one of the primary methods of mass measurements for the Roman telescope. Yet, mass measurements of only two events (OGLE-2003-BLG-235 and OGLE-2005-BLG-071) have been done using the color-dependent centroid shift method so far. The accuracy of the measurements using this method are neither completely known nor well studied. The agreement of the Keck and HST results, as shown in this paper, is very important because this agreement confirms the accuracy of the mass measurements determined at a small lens-source separation using the color-dependent centroid shift method. It also shows that with >100 high resolution images, the Roman telescope will be able to use color-dependent centroid shift at a 3–4 yr time baseline and produce mass measurements. We find that OGLE-2003-BLG-235 is a planetary system that consists of a $2.34 \pm 0.43 M_{\rm Jup}$ planet orbiting a $0.56 \pm 0.06 M_{\odot}$ K-dwarf host star at a distance of 5.26 ± 0.71 kpc from the Sun.

Unified Astronomy Thesaurus concepts: Gravitational microlensing exoplanet detection (2147); Infrared astronomy (786)

1. Introduction

Gravitational microlensing is unique in its ability to detect low mass exoplanets (Bennett & Rhie 1996) beyond the snow line (Gould & Loeb 1992), where the formation of giant planets is thought to be most efficient (Lissauer 1993; Pollack et al. 1996). The Roman Galactic Exoplanet Survey (RGES) was selected in the 2010 decadal survey (Bennett et al. 2010a; Spergel et al. 2015) to utilize this uniqueness and measure exoplanet demographics beyond the reach of the Kepler mission. The aim of this survey was to detect low mass planets beyond the snow line of their hosts and measure the masses of the hosts and the planets. The high resolution capability of the Roman telescope will measure the masses of both the hosts and the planets. Currently, as part of a precursor study for RGES, we are developing mass measurement methods (e.g., software for color-dependent centroid shifts) for the exoplanets that are detected from the ground.

OGLE-2003-BLG-235Lb was the first microlensing exoplanet to be discovered (Bond et al. 2004), as well as the first event

Original content from this work may be used under the terms of the Creative Commons Attribution 4.0 licence. Any further distribution of this work must maintain attribution to the author(s) and the title of the work, journal citation and DOI.

with mass measurements of the host star and the planet (Bennett et al. 2006). The lens host star is extremely faint when the source is magnified at its peak. Hence, the lens cannot be detected during this peak time of the microlensing event. However, years later, the source and lens have moved away from each other and the source is no longer magnified. At this point, these two stars can be detected in high angular resolution images. If the source and lens are partially or fully resolved in the image, then we observe the two stars appearing elongated and we call this image elongation. We can easily detect the two stars in the image-elongation method and measure their masses. If the lens and source are not resolved but they have very different colors, then they can still be detected in the high resolution images. For example, if the lens is redder than the source, then the centroid of the flux of these two stars will shift from being closer to the lens in the red passband to being closer to the source in the blue passband. By measuring this centroid shift based on the color differences of the stars (which is called the color-dependent centroid shift), we can detect the lens and measure the masses of the host and its planet. As Bennett et al. (2007) points out, the S/N of the image-elongation method scales as $(\Delta x)^2$, whereas the S/N of the color-dependent centroid shift scales as $(\triangle x)$. Note that $(\triangle x)$ is the lens-source separation in this case. Hence, as long as the colors of the

Department of Earth and Planetary Science, Graduate School of Science, The University of Tokyo, 7-3-1 Hongo, Bunkyo-ku, Tokyo 113-0033, Japan ¹⁰ Instituto de Astrofísica de Canarias, Vía Láctea s/n, E-38205 La Laguna, Tenerife, Spain Received 2022 August 27; revised 2023 March 10; accepted 2023 March 27; published 2023 April 19

source and lens stars differ significantly, this method should measure small separation values more precisely than the imageelongation method. This is the main advantage of the colordependent centroid shift method over the image-elongation method.

Bennett et al. (2006) observed the event with HST Advanced Camera for Surveys (ACS) instrument only 1.78 yr after the peak of the event, which was about 2003 July 30. The event was observed in three passbands (i.e., B, V, and I) to measure the color-dependent centroid shifts between the three different passbands. The foreground lens (host star) is brighter in red passbands and fainter in blue passbands, which causes the centroid of the lens-source flux to shift between red to blue passbands. The measurement of this centroid shift enabled the measurement of the microlens host and planet masses for the first time.

The mass measurement that we present for this study has the second shortest time gap between the peak of the event and the follow-up observation. OGLE-2005-BLG-071, with 0.84 yr gap, has the shortest time gap between the peak of the event and the follow-up observations (Bennett et al. 2020a). In the current paper, we confirm the 2006 color-dependent centroid shift results and the mass measurements with our 2018 Keck observations. We observe the event with Keck NIRC2 Adaptive Optics (AO) in 2018 and detect the lens host star separated from the source. We measure the lens-source relative proper motion, and predict the color-dependent centroid shift in 2005 data and compare with Bennett et al.'s (2006) work. We also measure the lens properties independently from the 2018 Keck data and use them to confirm the masses obtained from the 2006 paper. This work is important because this will be one of the primary methods of measuring the mass of the host stars and the planets with the Nancy Grace Roman Space Telescope (hereafter, Roman telescope; formerly WFIRST) mission, which is NASA's next astrophysics flagship mission to follow the James Webb Space Telescope (JWST).

The Roman telescope (Spergel et al. 2015) includes the Roman Galactic Exoplanet Survey (RGES; Penny et al. 2019), which will detect and measure the mass of hundreds of exoplanets in orbits extending from the habitable zone to infinity (i.e., unbound planets). The microlens exoplanets that are discovered by the Roman telescope will not require followup observations because the Roman observations will also have high enough angular resolution to detect the lens (and planetary host) stars (Bennett et al. 2007). The RGES will observe the galactic bulge in six to eight epochs across the 5 yr time-span. Hence, the maximum time separation between two epochs will be about \sim 4.5 yr. This happens because, in spite of the prime mission being 5 yr long, the time difference between the first and the last galactic bulge season will be about 4.5 yr. For example, a planetary event that was detected in the first epoch will be going through lens-source separation in the final epoch. So the masses of this system can be measured using the centroid shift method. However, this color-dependent centroid shift method for small separations of the lens and the source is not confirmed, except for one event (Bennett et al. 2020a). Very few color-dependent centroid shift measurements have been done, some of them with more than 4.5 yr after the peak of the event. Hence, confirming such a color-dependent centroid shift measurement, especially from such a small time separation, is important because it will demonstrate that RGES can properly conduct mass measurements.

This event is observed as part of our NASA Keck Key Strategic Mission Support (KSMS) program, whose main purpose is to refine the mass measurement method and optimize the Roman exoplanet microlensing survey observing program. We are conducting a systematic exoplanet microlensing event high angular resolution follow-up program to detect and determine the masses of the exoplanet host stars with our NASA Keck KSMS program (Bennett 2018). This is supplemented by HST observations (Bhattacharya et al. 2019b) for host stars that are most likely to be detected with the color-dependent centroid shift method (Bennett et al. 2006). This program has already revealed a number of microlens exoplanet host stars that are resolved from the source stars (Bennett et al. 2020a; Vandorou et al. 2020; Blackman et al. 2021; Terry et al. 2021) and others that are still blended with their source stars but show a significant elongation due to a lens-source separation somewhat smaller than the size of the point-spread function (PSF; Bennett et al. 2007, 2015; Bhattacharya et al. 2018). This program has also recently provided mass upper limits of a Jovian planet orbiting a White Dwarf host. Another purpose of our NASA KSMS program is to confirm measurements of the small lens-source separation with under-sampled pixels (e.g., Bennett et al. 2020a). In this paper, we will confirm the small lens-source separation measured by under-sampled HST pixels with Keck high angular resolution images.

This paper is organized as follows. Section 2 revisits the ground based seeing limited photometry data from 2003 and reanalyzes the light-curve modeling. The main purpose of this reanalysis is to obtain the MCMC chains that are necessary to calculate the uncertainties in the mass measurements. The lightcurve modeling from Bond et al. (2004) did not provide these MCMC chains. Section 3 describes the details of our high resolution follow-up observations and the reduction of the AO images. In the next two sections, we show the process of identifying the host star (which is also the lens) and the source star. In Section 7, we predict the color-dependent centroid shifts between B, V, and I passbands in the 2005 data based on the geocentric relative lens-source proper motion from the lens and source identification in the 2018 Keck data. Note that from here on we address the results of Bennett et al. (2006) as the analysis of the 2006 paper, even though it refers to the analysis of 2005 Hubble data. We show that this prediction matches with the centroid shift measurements in Bennett et al.'s (2006) paper. Finally, in Sections 6 and 8, we discuss the exoplanet system properties and the implications of its mass and distance measurement.

2. Revisiting Photometry and Light-curve Modeling

The light-curve modeling of this event was first published in Bond et al. (2004). However, the OGLE III data used for this modeling was not calibrated until 2010. Hence, in this paper, we perform the remodeling of the light-curve photometry with calibrated OGLE III V data. This was done using Bennett's (2010) modeling code. The resulting model parameters are given in Table 1. The model parameters that are in common with single lens events are the Einstein radius crossing time, $t_{\rm E}$, the time, $t_{\rm 0}$, and distance, $u_{\rm 0}$, of closest alignment between the source and the lens center-of-mass, where $u_{\rm 0}$ is given in units of the Einstein radius. There are four additional parameters for binary lens systems: the star-planet separation in Einstein radius units, s, the angle between the lens axis and the source

Table 1Best Fit Model Parameters

parameter	Values
$t_{\rm E}$ (days)	61.2 ± 2.2
$t_0 \text{ (HJD')}$	2848.04 ± 0.11
u_0	-0.13 ± 0.61
S	1.12 ± 0.43
α (rad)	0.76 ± 0.15
$q \times 10^{-3}$	3.99 ± 0.48
t_* (days)	0.061 ± 0.004
$\theta_{\rm E}$ (mas)	0.59 ± 0.07
V_S	21.23 ± 0.05
I_S	19.72 ± 0.05
$\mu_{\rm rel,G}$ (mas yr ⁻¹)	3.48 ± 0.14

trajectory, α , the planet-star mass ratio, q, and the source radius crossing time, t_* , which are needed for events, like most planetary events, that have very sharp intrinsic light-curve features that resolve the angular size of the source star. The brightness of the source star, $f_{\rm Si}$ and blended stars, $f_{\rm Bi}$ are also fitted to the observed brightness for each passband, i, using the formula $F_i(t) = f_{\rm Si}A(t) + f_{\rm Bi}$, where A(t) is the magnification from the model and $F_i(t)$ is the observed flux in the $i^{\rm th}$ passband. Because this is a linear equation, $f_{\rm Si}$ and $f_{\rm Bi}$ can be solved for each model in the Markov chain (Rhie et al. 1999).

Another improvement is that Nataf et al. (2013) has provided a more accurate determination of the properties of the red clump giants that are used to determine the dust extinction in the foreground of the source. This has resulted in a more accurate source radius and a relative lens-source proper motion, $\mu_{\text{rel,G}}$. The $\mu_{\text{rel,G}}$ prediction is important because it can be used to confirm our planetary interpretation of the light curve (Batista et al. 2015; Bennett et al. 2015).

3. Follow-up Observations

3.1. Wide Camera

The event was observed with the Keck Adaptive Optics (AO) NIRC2 (Wizinowich et al. 2000) instrument during the early morning of 2018 August 5. Five dithered exposures, each of 30 s, were taken in the K_S short passband (hereafter, K band) with the wide camera. Each wide camera image covers a 1024×1024 square pixel area, and each pixel size is about 39.686×39.686 mas. These images were flat field and dark current corrected using standard methods, and then stacked using the SWarp Astrometics package (Bertin et al. 2002). The details of our methods are described in Batista et al. (2014). We used aperture photometry method on these wide images with SExtractor software (Bertin & Arnouts 1996). These wide images were used to detect and match 22 bright isolated stars to the VVV catalog (Minniti et al. 2010) for calibration purposes. The average FWHM of this wide camera stack image is 90 mas. Note that the lens and source were not resolved in the 2018 wide camera images. As a result, we need NIRC2 narrow camera images to resolve and to identify the lens system.

3.2. Narrow Camera

This event was also observed with the Keck NIRC2 narrow camera on 2018 August 5 in the *K*-band using laser guide star adaptive optics (LGSAO). The main purpose of these images is to resolve the lens host star from the source star. Sixteen

dithered observations were taken with 60 s exposures. The images were taken with a small dither of 0.7" at a position angle (P.A.) of 0° with each frame consisting of three co-added 20 s integrations. The average FWHM of these images is \approx 50 mas. For the reduction of these images, we used nine dark images of 60 s exposure time and 10 K-band dome flats taken with narrow camera on the same day as the science images. There were five dome flat images with the lamp on and five more images with the lamp off, each with 60 s exposure time. Also at the end of the night, we took 31 sky images using a clear patch of sky at a (R.A., decl.) of (20:29:57.71, -28.59.30.01) with an exposure time of 30 s each. All of these images were taken with the K band filter. These images were used to flat field, bias subtract, and remove bad pixels and cosmic rays from the 11 raw science images. The strehl ratio of these clean images varied over the range 0.21–0.41. Finally these clean raw images were distortion corrected, differential atmospheric refraction corrected, and stacked into one image (Lu 2008, 2022). We used the stacked image for the final photometry and astrometry analysis.

There are 1024×1024 pixels in each narrow camera image with each pixel subtending 9.942 mas (Yelda et al. 2010; Service et al. 2016) on each side. Since the small field of these narrow images covers only a few bright stars, it is difficult to directly photometrically calibrate them to VVV. On the contrary, wide images cover 1024×1024 pixels with each pixel subtending 39.686 mas on each side. So we use the wide camera K stack image that was already calibrated to VVV (see above Section 3.1) to calibrate the narrow camera images. The wide and narrow images were taken in the same filter, and hence we did not need to do any filter conversion. This gives us the brightness calibration between the stacked narrow camera image to VVV image. The photometry used for the narrow camera image calibration is from DAOPHOT analysis (Section 4).

4. Keck Narrow Camera Image Analysis

In this section, we use DAOPHOT (Stetson 1987) to construct a proper empirical PSF model to identify the two stars (the lens and the source) in the narrow stack images. We started our analysis with the 2018 Keck narrow camera images. We used the same method as Bhattacharya et al. (2018) to build PSF models for the narrow camera stack images. We built these PSF models in two stages. In the first stage, we ran the FIND and PHOT commands of DAOPHOT to find all of the possible stars in the image. In the second stage, we used the PICK command to build a list of bright (K < 18.5) isolated stars that can be used to construct our empirical PSF model. Our target object was excluded from this list of PSF stars because it is expected to consist of two stars that are not in the same position. From this list, we selected the four nearest stars to the target that had sufficient brightness, and we built our PSF model from these stars. We chose only the nearest stars to avoid any effect of PSF shape variations across the image.

Once we had built the PSF model, we were able to fit all of the stars with this model. This step produced the single star residual fit for the target that is shown in Figure 1(C). Inspection of this residual image from the single star fit indicates that there is an additional star near the target object. Therefore, we tried fitting the region of the target object with a dual star model. The dual star fits produced a smoother residual than the single star fit, as shown in Figure 1(D). The results of

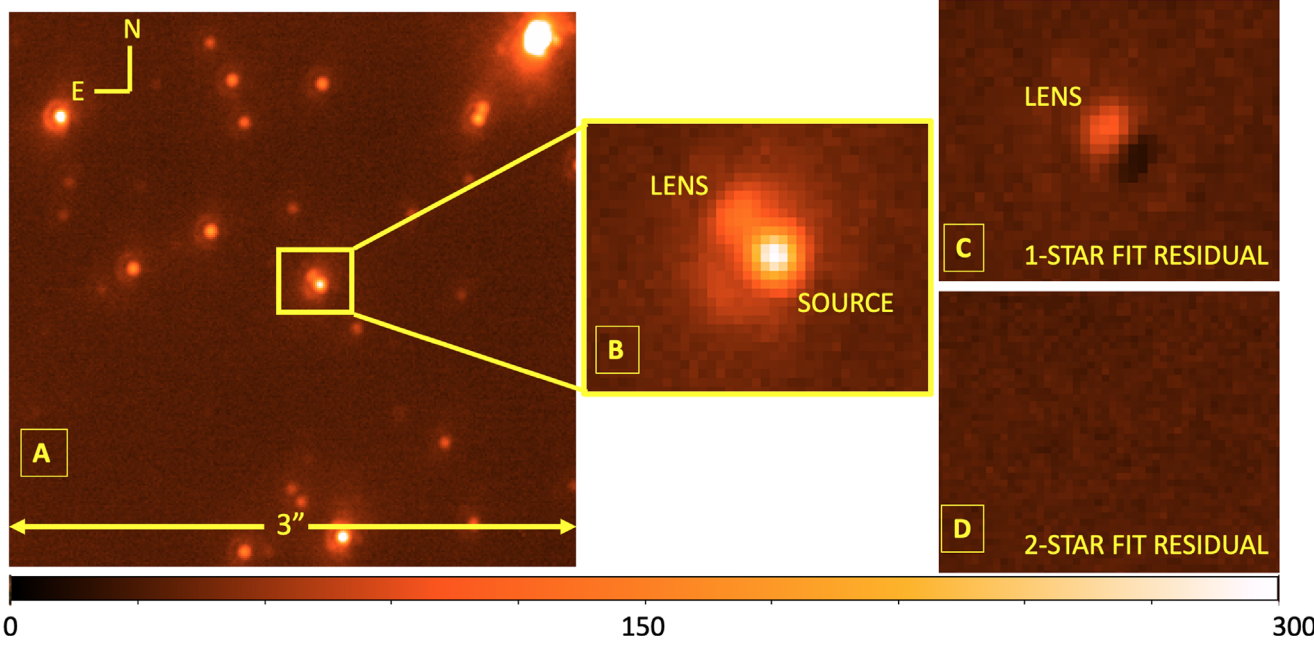


Figure 1. Panel (A): A 3'' section of the stack image of 16 Keck K-band images, taken with the narrow camera, with the yellow square indicating the target. Panel (B): A close-up of the target object. The source and lens positions are obtained from the best fit dual star PSF model. Panel (C): The residual image after subtracting the best fit single star PSF model. The residual shows a clear indication of the presence of an additional star East of the target. Panel (D): The residual image after subtracting the best fit dual star PSF model. This shows a smooth residual, confirming the second star at separation of \sim 54 mas. (C) and (D) use the same photometry scale

Table 2
Source and Lens Photometry and Astrometry from the 2018 Keck Data

Calibrated Magnitudes		Lens- Source Separation(mas)		
Source	Lens	East	North	total
17.76 ± 0.06	19.20 ± 0.11	37.07 ± 0.18	38.57 ± 0.45	53.5 ± 0.51

Note. The separation was measured 15.01 yr after the peak of the event in the *K* band. The follow-up observation was taken on 2018 August 5 and the peak of the microlensing light-curve event was on 2003 July 30.

these dual star fits are given in Tables 2 and 3. Both the single star and dual star fits were done using the Newton-Raphson method of standard DAOPHOT. There is a minor wing-like feature to the south and east of the source star in Figure 1(B). However, this feature is seen in all of the nearby stars in the image and has been easily taken care of by the empirical PSF that is built from the nearby star brightness profiles. Hence, in Figures 1(C) and (D), this feature is subtracted clearly in the residual images. Keck PSFs are often not perfectly round due to the instability of the atmosphere. However, the method of empirical PSF building from the nearby stars seems to compensate for that and does a proper PSF fitting, even when the PSFs are not perfectly round. As we discuss in Section 5, we identify the brighter of the two stars as the source for the OGLE-2003-BLG-235 microlensing event, and the fainter star to the northeast as the lens and planetary host star.

We calculated the error bars using the Jackknife method (Quenouille 1949, 1956; Tukey 1958; Tierney & Mira 1999) following Bhattacharya et al. (2021). This method is able to measure the variance due to the PSF variations in the individual images. There were a total of 16 clean Keck images. In this method, we built 16 different stacks of 15 images by removing one of the 16 images each time. These 16 images are then analyzed with DAOPHOT to build empirical PSFs for each stack image. Next, the target in each image is fit with the dual

 Table 3

 Measured Lens-source Relative Proper Motion

$\mu_{\rm rel,H}({ m mas~yr}^{-1})$			$\mu_{\rm rel,G}({ m mas~yr}^{-1})$	
			Measured	From light
$\mu_{ m rel,H,E}$	$oldsymbol{\mu}_{ ext{rel}, ext{H}, ext{N}}$	$ oldsymbol{\mu}_{ m rel,H} $	from Keck	curve
2.47 ± 0.01	2.57 ± 0.03	3.56 ± 0.08	3.31 ± 0.06	3.48 ± 0.15

star PSF models. Once we have 16 sets of positions and flux of lens and source, the sample mean and the standard deviation of the parameters are used for the statistics. The standard error of a parameter *x* in Jackknife is given by:

$$SE(x) = \sqrt{\frac{N-1}{N} \sum (x_i - \bar{x})^2}.$$
 (1)

The x_i represents the value of the parameter measured in each of the combined image and \bar{x} represents the mean of the parameter x from all the N stacked images. This Equation (1) is the same formula as the sample mean error, except that it is multiplied by $\sqrt{N-1}$. These error bars are reported in Table 2. The error bars in Table 3 are based on the error bars in Table 2 because the Heliocentric lens-source relative proper motion, $\mu_{\rm rel,H}$, is proportional to the lens-source separation.

5. Interpreting the Keck Results

In the previous sections, we have referred to the Keck images of the source and lens (and planetary host) stars. We will now discuss the analysis that shows that our identifications of the source and lens stars are correct. Based on these identifications, we compare our 2018 Keck results to the 2006 result (Bennett et al. 2006) and we show that they are consistent in Section 6.

5.1. Confirming the Source Star Identification

Our reanalysis of the light-curve model of this event (with improved OGLE III calibration) showed the best fit model gives the source brightness $I_S = 19.72 \pm 0.05$ $V_S = 21.23 \pm 0.05$. The average extinction and reddening of the red clump stars within 2.5 of the target are $A_I = 1.22$ and E (V-I) = 0.92, as calculated from the OGLE-III photometry catalog (Szymański et al. 2011). This means the extinction corrected source magnitudes are $I_{S,0} = 18.49 \pm 0.06$ and $V_{S,0} = 19.09 \pm 0.06$. The extinction corrected color is $(V-I)_{S,0} = 0.60 \pm 0.04$. From the color-color relation of Kenyon & Hartmann (1995), $(V - I)_{S,0} = 0.60$ corresponds to the dereddened colors of $(V - K)_{S,0} = 1.28$. So the extinction corrected source brightnesses in K is $K_{S,0} = 17.81 \pm 0.06$ including a 5% uncertainty in the color-color relation. The extinction in the K band is $A_K = 0.13$ (Dutra et al. 2003), and hence the expected K band calibrated magnitude of the source is $K_S = 17.94 \pm 0.08$.

The dual star fits to 2018 narrow camera Keck images imply that the two stars located at the position of the target are resolved. The best dual star fit yielded two stars with calibrated K magnitudes of 17.76 ± 0.06 and 19.20 ± 0.11 . The error bars are calculated using the Jackknife method, as discussed in Section 4. The brighter star from these dual star fits matches the expected source magnitudes that were derived earlier. Hence, we identify the brighter star as the source star and the fainter star as the potential lens star.

5.2. Determination of Relative Lens-source Proper Motion

We will determine the relative proper motion between the lens candidate and the source star. In this subsection, we will measure the heliocentric relative proper motion from narrow Keck images and then transform that to a geocentric frame. We then compare the measured geocentric relative proper motion to the predicted relative lens-source proper motion from the light curve. This will help us to later confirm that the second star is indeed the lens star. Given that in the next section we show that this possible lens star is the lens, we will call the relative proper motion a relative lens-source proper motion from now for simplicity.

The two stars are separated by slightly more than the FWHM of the K band image, with the separations given in Table 2. The measured separations can be used to compute the lens-source relative proper motion, $\mu_{\rm rel}$, which can be compared with the $\mu_{\rm rel}$ prediction from the light curve. However, this issue is complicated by the fact that the lens-source separation measurements determine the relative proper motion in a Heliocentric frame, $\mu_{\rm rel,H}$, while the light curve measures the relative proper motion in an inertial Geocentric reference frame, $\mu_{\rm rel,G}$, that moves with the Earth's velocity at the time of the event. The relationship between these reference frames is given by Equation (2).

Our high resolution observations of 2018 were taken ~ 15.01 yr after the microlensing event magnification peak. Since these images were taken almost exactly 15 yr after the microlensing magnification, we do not need to consider the relative position of the Earth with respect to the Sun when determining the heliocentric lens-source relative proper motion from the measured separations in the Keck images.

At the time of peak magnification, the separation between lens and source was $\sim |u_0\theta_{\rm E}| \sim 0.017$ mas. Hence, by dividing the measured separation by the time interval of 15.01 yr, we obtain the heliocentric lens-source relative proper motion, $\mu_{\rm rel, H}$. A comparison of these values from our independent dual star fits for the K band is shown in Table 3, note that the error bars are estimated from the Jackknife method.

Our light-curve models were done in a geocentric reference frame that differs from the heliocentric frame by the instantaneous velocity of the Earth at the time of peak magnification because the light-curve parameters can be determined most precisely in this frame. However, this also means that the lens-source relative proper motion that we measure with follow-up observations is not in the same reference frame as the light-curve parameters. This is an important issue because, as we show below (see Section 6), the measured relative proper motion can be combined with brightness of the source star to determine the mass of the lens system. The relationships between the relative proper motions in the heliocentric and geocentric coordinate systems are given by Dong et al. (2009):

$$\mu_{\text{rel},H} = \mu_{\text{rel},G} + \frac{\nu_{\oplus}\pi_{\text{rel}}}{\text{AU}},$$
 (2)

where v_{\oplus} is the projected velocity of the earth relative to the Sun (perpendicular to the line-of-sight) at the time of peak magnification.

The projected velocity for OGLE-2003-BLG-235 is $v_{\oplus E,N} = (24.53, -1.304) \text{ km/sec} = (5.17, -0.28) \text{ au yr}^{-1}$ at the peak of the microlensing. The relative parallax is defined as $\pi_{\text{rel}} \equiv (1/D_L - 1/D_S)$, where D_L and D_S are lens and source distances. Hence, Equation (2) can written as:

$$\mu_{\text{rel,G}} = \mu_{\text{rel,H}} - (5.17, -0.28) \times (1/D_L - 1/D_S)$$
 (3)

Since $\mu_{\rm rel,H}$ is already measured in Table 3, Equation (3) yields the geocentric relative proper motion, $\mu_{\rm rel,G}$ as a function of the lens distance. Now, at each possible lens distance, we can use the $\mu_{\rm rel,G}$ value from Equation (3) to determine the angular Einstein radius, $\theta_{\rm E}=\mu_{\rm rel,G}t_{\rm E}$. Since we already know the $\theta_{\rm E}$ value from the light-curve models, we can use that here to constrain the lens distance and relative proper motion. Using this method, we determined the relative proper motion to be $\mu_{\rm rel,G}=3.31\pm0.06$. This value is consistent with the predicted $\mu_{\rm rel,G}=3.48\pm0.15$ mas yr $^{-1}$ from the light-curve models.

5.3. Confirmation of the Host Star Identification

We can confirm our identification of the lens star only if the measured lens source relative proper motion is consistent with the predicted one from the light curve. Note that, the measured relative proper motion in Keck images is in Heliocentric frame. To compare the measured relative proper motion to the light-curve prediction of $\mu_{\rm rel,G} = 3.48 \pm 0.15~{\rm mas~yr}^{-1}$, we used Equation (2) to convert between the Geocentric and Heliocentric coordinate systems in Section 5.2. This requires

 Table 4

 Comparison of Measurement of Planetary System Parameters from 2018 vs. 2005 Data

Parameter	Units	2018	2005
Geocentric lens-source relative proper motion, $\mu_{\rm rel,G}$	mas yr ⁻¹	3.31 ± 0.06	3.3 ± 0.4
Host star mass, M_{host}	M_{\odot}	0.56 ± 0.06	$0.63^{+0.07}_{-0.09}$
Planet mass, m_p	$M_{ m Jup}$	2.34 ± 0.43	$2.6_{-0.06}^{+0.8}$
Host star-planet 3D separation, a_{3D}	AU	$4.0^{+2.1}_{-0.7}$	$4.3^{+2.5}_{-0.08}$
Lens distance, D_L	kpc	5.26 ± 0.71	$5.8^{+0.6}_{-0.7}$

knowledge of the source and lens distances, and we do this comparison inside our Bayesian analysis (presented in Section 6), which combines the Markov chains of the light-curve models with the constraints from the Keck observations and the Galactic models. As shown in Table 3, the measured and predicted $\mu_{\rm rel,G}$ are consistent within 1σ . This shows that the faint star in Table 2 is the lens.

In addition, Table 4 shows the measured relative proper motion in 2006 HST analysis paper of this event. The fainter star was much closer to the source in 2005 data and at a much farther distance in 2018 data. The consistency between 2005 and 2018 measurements with the same lens-source relative motion shows that it is indeed this star that is moving away from the source. This proves that this faint star is the lens and not a nearby unrelated star. Now that we have identified the lens star, the details of mass measurement and its properties are given below.

6. Lens Properties

Mass measurements of microlensing exoplanets and their hosts can be done by solving a minimum of two of the three mass-distance relations. Measurements of the angular Einstein radius, $\theta_{\rm E}$, and the microlensing parallax amplitude, $\pi_{\rm E}$, can each provide mass-distance relations (Bennett 2008; Gaudi 2012),

$$M_L = \frac{c^2}{4G} \theta_E^2 \frac{D_S D_L}{D_S - D_L} = \frac{c^2}{4G} \frac{AU^2}{\pi_E^2} \frac{D_S - D_L}{D_S D_L}.$$
 (4)

 D_L and D_S are distances to the lens and the source, respectively. These can be combined to yield the lens mass in an expression with no dependence on the lens or source distance,

$$M_L = \frac{c^2 \theta_{\rm E} A U}{4G \pi_{\rm E}} = \frac{\theta_{\rm E}}{(8.1439 \text{ mas}) \pi_{\rm E}} M_{\odot}.$$
 (5)

The angular Einstein radius can be measured for most planetary microlensing events because most planetary events have finite source effects that allow the measurement of the source radius crossing time, t_* . The angular Einstein radius is then given by $\theta_{\rm E} = \theta_* t_{\rm E}/t_*$, where $t_{\rm E}$ is the Einstein radius crossing time and θ_* is the angular source radius, which can be determined from the source brightness and color (Kervella et al. 2004; Boyajian et al. 2014). As a result, the measurement of π_E for planetary events usually results in mass measurements. Unfortunately, the orbital motion of the Earth allows π_E to be determined for only a relatively small subset of events, such as the ones that have very long durations (e.g., Gaudi et al. 2008; Bennett & Rhie et al. 2010b), long duration events with bright source stars (e.g., Muraki et al. 2011), and events with special lens geometries (e.g., Sumi et al. 2016). The microlensing parallax program using the Spitzer space telescope at ~ 1 au from Earth has recently expanded the number of events with microlensing parallax measurements (Udalski et al. 2015; Street et al. 2016), but recent studies have indicated that systematic errors in the *Spitzer* photometry can affect some of the Spitzer $\pi_{\rm E}$ measurements (Dang et al. 2020; Gould et al. 2020; Koshimoto & Bennett 2020).

The masses of the largest number of planetary microlensing events can be determined by detecting the exoplanet host star as it separates from the background source star. However, due to the high stellar density in the fields where microlensing events are found, it is necessary to use high angular resolution adaptive optics (AO) or HST observations to resolve the (possibly blended) lens and source stars from other, unrelated stars. Unfortunately, this is not sufficient to establish a unique identification of the lens (and planetary host) star (Bhattacharya et al. 2017; Koshimoto et al. 2020), and so it is necessary to confirm that the host star is moving away from the source star at the predicted rate (Batista et al. 2015; Bennett et al. 2015). For this reason, we analyzed and confirmed in the previous section that the additional flux on top of the source is indeed the host lens star.

To obtain good sampling of light-curve model parameters that are consistent with our photometric constraints and astrometry, we apply the following constraints, along with Galactic model constraints when summing over our light-curve modeling MCMC results to determine the final parameters. The proper motion vectors of $\mu_{\rm rel,H}$ and the lens magnitudes are constrained according to Tables 1 and 3. The $\mu_{\rm rel,H}$ constraints are applied to the Galactic model and the lens magnitude constraints are applied when combining the MCMC light-curve model results with the Galactic model. The lens magnitude constraints require the use of a massluminosity relation. We built an empirical mass-luminosity relation following the method presented in Bennett et al. (2018). This relation is a combination of mass-luminosity relations for different mass ranges. For $M_L \geqslant 0.66 \, M_{\odot}$, $0.54 \, M_{\odot} \geqslant$ $M_L \geqslant 0.12 \, M_{\odot}$, and $0.10 \, M_{\odot} \geqslant M_L \geqslant 0.07 \, M_{\odot}$, we use the relations of Henry & McCarthy (1993), Delfosse et al. (2000), and Henry et al. (1999), respectively. Between these mass ranges, we linearly interpolate between the two relations used on the boundaries. That is, we interpolate between the Henry & McCarthy (1993) and the Delfosse et al. (2000) relations for $0.66 \, M_{\odot} > M_L > 0.54 \, M_{\odot}$, and we interpolate between the Delfosse et al. (2000) and Henry et al. (1999) relations for $0.12 \, M_{\odot} > M_L > 0.10 \, M_{\odot}$. When using these relations, we assume a 0.05 magnitude uncertainty.

For the mass-luminosity relations, we must also consider the foreground extinction. At a Galactic latitude of $b = -4^{\circ}.7009$, most of the dust is likely to be in the foreground of the lens unless it is very close to us. We quantify this with a relation relating the extinction of the foreground of the lens to the extinction in the foreground of the source. Assuming a dust

scale height of $h_{\rm dust} = 0.10 \pm 0.02\,$ kpc, we have

$$A_{i,L} = \frac{1 - e^{-|D_L(\sin b)/h_{\text{dust}}|}}{1 - e^{-|D_S(\sin b)/h_{\text{dust}}|}} A_{i,S}, \tag{6}$$

where the index i refers to the passband: V, I, H, or K.

These dereddened magnitudes can be used to determine the angular source radius, θ_* . With the source magnitudes that we have measured, the most precise determination of θ_* comes from the (V-I), I relation. We use

$$\log_{10}[2\theta_*/(1\text{mas})] = 0.501414 + 0.419685(V - I)_{s0} - 0.2 I_{s0},$$
 (7)

which comes from the Boyajian et al. (2014) analysis, but with the color range optimized for the needs of microlensing surveys (Bhattacharya et al. 2016).

We apply the K-band mass-luminosity relations to each of the models in our Markov chains using the mass determined by the first expression of Equation (4), using the θ_E value determined from $\theta_{\rm E} = \theta_* t_{\rm E}/t_*$, where $t_{\rm E}$ and t_* are light-curve parameters given in Table 1. We can then use the Keck *K*-band measurements of the lens star brightness from Table 2 to constrain the lens brightness, including both the observational uncertainties listed in Table 2 and the 0.05 mag theoretical uncertainty that we assume for our empirical K-band massluminosity relations. We solve the first expression of Equation (4) along with the mass–luminosity relations. While solving, we assume the source distance $D_S = 8.57 \pm 1.42 \,\mathrm{kpc}$. We solve this for every MCMC model and we sum over our MCMC results using the Galactic model employed by Bennett et al. (2014) as a prior, weighted by the microlensing rate and the measured $\mu_{\rm rel,H}$ values given in Table 3. The results of our final sum over the Markov chain light-curve models are given in Table 4 and Figure 2. This table gives the mean and rms uncertainty plus the central 95.4% confidence interval range for each parameter except the 3D separation, a_{3D} , where we give the median and the central 68.3% confidence interval instead of the mean and rms. The host mass is measured to be $M_{\rm host} = 0.56 \pm 0.06 M_{\odot}$, a K dwarf star, orbited by a super-Jupiter mass planet, $M_{\rm Planet} = 2.34 \pm 0.43 M_{\rm Jup}$.

Figure 2 and Table 4 show the comparison between mass measurements from HST and light-curve model, and the measurements only from Keck. As we can see from Table 4, the mass and distance measurements from both 2006 and 2018 data are consistent within 1σ .

7. Confirming the Centroid Shift Measurement

The lens was detected in Bennett et al.'s (2006) paper by measuring the centroid shifts between B, V, and I passbands in the HST data. This data was taken only 1.78 yr after the peak of the event. Figure 2 of Bennett et al. (2006) shows the measurements of the centroid shift in different bands. The x and y axes are aligned with RA and Dec. These values are also given in the last two columns of Table 5.

As the lens separates out from the source star, it is detected in the 2018 Keck data. This detection is independent of the detection in 2006 HST data. To confirm the centroid shift measurements done in the previous paper, we predict the centroid shifts in B-I, B-V, and V-I passbands. The $\mu_{\rm rel,H}$ is 2.4674 ± 0.0121 mas yr⁻¹ and 2.5670 ± 0.0215 mas yr⁻¹ for East and North. This gives the predicted separation at 1.78 yr is $dE=4.3920 \pm 0.0215$ mas and $dN=4.5693 \pm 0.0532$ mas.

Since we know the lens-source flux ratio in three passbands B, V, and I from Bennett et al. (2006), we predicted the centroids at a separation of $dE = 4.3920 \pm 0.0215$ mas and $dN = 4.5693 \pm 0.0532$ mas in B, V, and I passbands. From this, we predicted the centroid shifts in B - I, V - I, and B - V passbands. These predictions are shown in Table 5.

Note that the B-I centroid shift matches pretty well with both components, within 1σ . The East component of the B-V centroid shift is also within 1σ but the North component is just outside 2σ . Both components of the V-I centroid shift are within 1σ and 2σ of the prediction. Note that it was shown in the Bennett et al.'s (2006) paper that the V centroid is too close to the I centroid and too far from the B centroid to be 100% consistent with normal stellar colors. This may be the reason B-V centroid shift in North component is just outside 2σ .

This is the second event with the confirmation of color-dependent centroid shift measurements. Bennett et al. (2020a) has confirmed the mass measurement of Dong et al. (2009), which was observed by HST only 0.84 yr after the peak of the event.

8. Discussion and Conclusions

OGLE-2003-BLG-235 was observed in 2018 to confirm the lens detection in the 2006 data that was done with centroid shift method. The color-dependent centroid shift method will be one of the primary methods of mass measurement of exoplanets and their hosts with the Roman telescope. In this paper, we wanted to demonstrate the feasibility of this method. We measured relative lens-source proper motion and the masses using 2018 Keck data, completely independent of Bennett et al.'s (2006) paper, and found that they are consistent. We predicted the centroid shifts based on the separation measured from 2018 data and found that they are consistent with the ones measured in the 2006 analysis. This shows that the color-dependent centroid shift method provides reliable results.

The color-dependent centroid shift mass measurement is a powerful tool when determining masses of systems where the lens and source are merely separated. Currently, this method is built and tested with 8-16 dithered images with HST and about 30 dithered images with Keck. In the Roman Galactic Exoplanet Survey, there will be six epochs spread out over 5 yr. The maximum time separation between the first epoch and the last epoch will be about 4.5 yr. Most of the events have an average 5 mas yr⁻¹ lens-source relative proper motion. Hence, for most of the events, the lens-source separation will be about \lesssim 22.5 mas. The pixel scale of the Roman telescope is 110 mas. Hence, the lens-source separation will be around ≤ 0.2 parts of the pixel. Comparing to the 2006 studies, the lens-source separation was 0.16 parts of the pixel of HST ACS camera. In addition, the Roman Galactic Exoplanet Survey will take a total of about 40,000 images in the wide band and 800 dithered images in each additional passband (two-one red and one bluer than wide F146) in each of the seven fields across six seasons. Each season consists of about 72 days of observations. So each field will have >100 dithered images in different passbands in each season. The analysis of this huge number of dithers will provide us a very well sampled PSF and yield a significantly higher photometric and astrometric precision compared to a handful of HST images. This advantage will aid immensely in obtaining mass measurements of the lens (host and exoplanet) with the color-dependent centroid shift method.

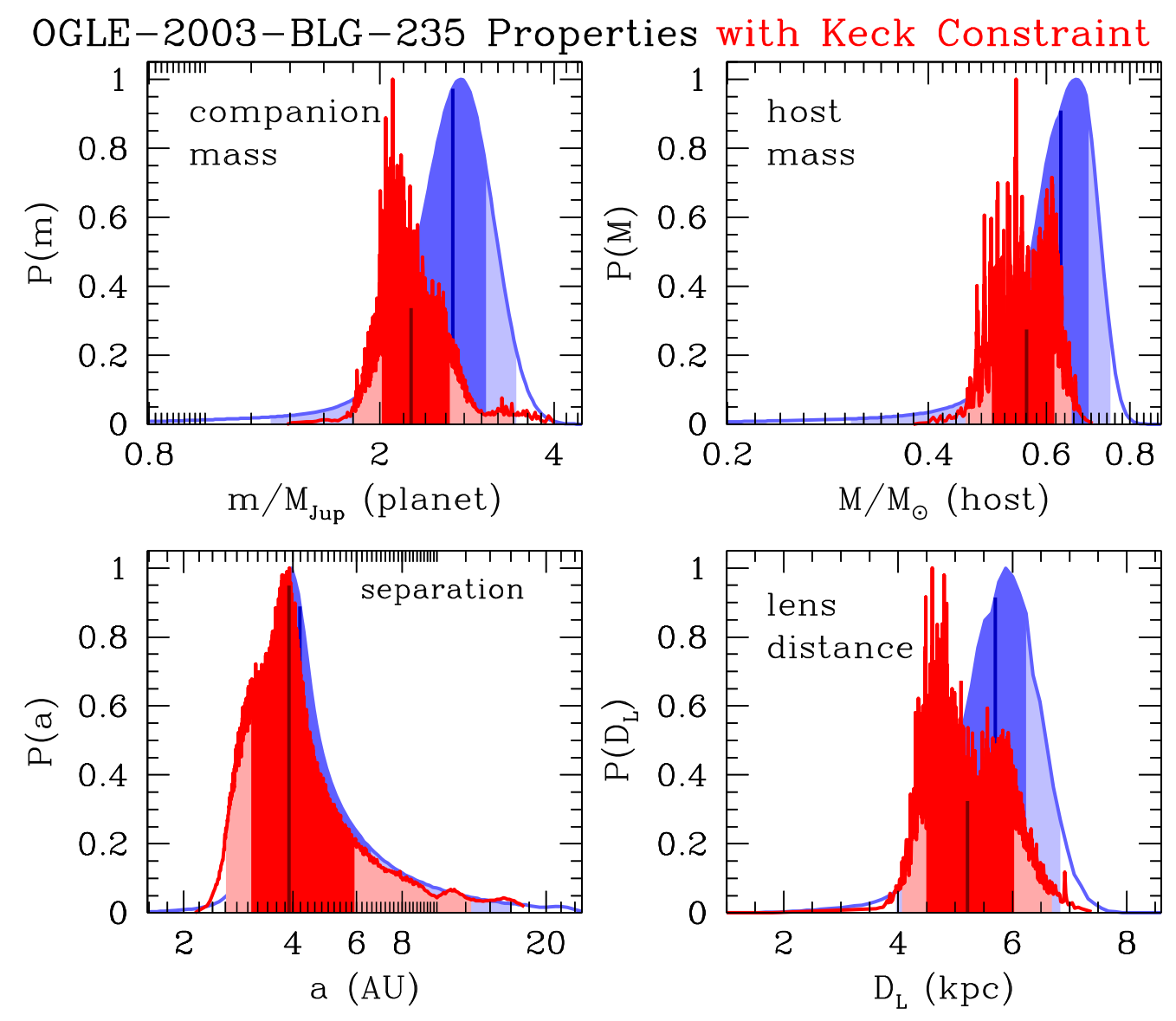


Figure 2. The Bayesian posterior probability distributions for the planetary companion mass, host mass, their separation, and the distance to the lens system are shown with the light-curve + HST constraints in blue (based on Bennett et al. 2006) and the constraints from our Keck follow-up observations in red. The central 68.3% of the distributions are shaded in darker colors (dark red and dark blue) and the remaining central 95.4% of the distributions are shaded in lighter colors. The vertical black line marks the median of the probability distribution of the respective parameters. The older results are smoother because they assume Gaussian uncertainties on the microlens model parameters, while new results include the full parameter distributions from the MCMC. This comparison shows the consistency of the 2018 mass measurement results from Keck to the 2005 mass measurement results with HST centroid shift measurements.

Table 5
The Prediction of Centroid Shift from 2018 Data vs. Actual 2006 Analysis

Passbands	Prediction Based on 2018 Data		HST Analysis from 2006	
	East	North	East	North
B-I	-0.52 ± 0.06	-0.54 ± 0.06	-0.26 ± 0.36	-0.62 ± 0.24
B-V	-0.14 ± 0.04	-0.14 ± 0.04	-0.21 ± 0.29	-0.61 ± 0.23
V-I	-0.38 ± 0.04	-0.39 ± 0.04	-0.05 ± 0.27	-0.01 ± 0.22

The color-dependent centroid shift method can also be utilized by joint Euclid-Roman survey (Bachelet et al. 2022) to measure the masses of RGES microlensing planets. In this proposed multiband survey, all of the RGES fields will be observed by Euclid a few yr before the launch of Roman. This brief and early Euclid survey will capture several future microlensing candidates where the lens and source are moving

toward each other before the peak of the microlensing event. When Roman detects the microlensing planetary events, the Euclid multiband microlensing data will show the lens and source as partially resolved and the color-dependent centroid shift method can be used to measure the host star mass. However, it should be noted that the Roman telescope itself will be able to measure the masses of significant numbers of the

microlensing planetary events using its high resolution capabilities. NASA requires RGES should be capable of determining the masses of, and distances to, host stars of 40% of the detected planets with a precision of 20% or better. This paper shows that it will be possible to detect masses and distances with a precision at par with the requirement.

This work made use of data from the Astro Data Lab at NSF's OIR Lab, which is operated by the Association of Universities for Research in Astronomy (AURA), Inc. under a cooperative agreement with the National Science Foundation. We also acknowledge the help of Dr. Peter Stetson on providing us with a feedback on our analysis of Keck data. The Keck Telescope observations and analysis was supported by a NASA Keck PI Data Award 80NSSC18K0793. The data presented herein were obtained at the W. M. Keck Observatory from telescope time allocated to the National Aeronautics and Space Administration through the agency's scientific partnership with the California Institute of Technology and the University of California. The Observatory was made possible by the generous financial support of the W. M. Keck Foundation. D.P.B., A.B., N.K., and S.K.T. were also supported by NASA through grant NASA-80NSSC18K0274 and by NASA award number 80GSFC17M0002. This work was supported by the University of Tasmania through the UTAS Foundation and the endowed Warren Chair in Astronomy and the ANR COLD- WORLDS (ANR-18-CE31-0002). This research was also supported in part by the Australian Government through the Australian Research Council Discovery Pro- gram (project number 200101909) grant awarded to Cole and Beaulieu. The work by N.K. is supported by JSPS KAKENHI grant No. JP18J00897. J.R.L. acknowledges support by the National Science Foundation under grant No. 1909641 and the Heising-Simons Foundation under grant No. 2022-3542. A.F.'s work was partly supported by JSPS KAKENHI grant No. JP17H02871.

ORCID iDs

```
David P. Bennett https://orcid.org/0000-0001-8043-8413
Jean Philippe Beaulieu https://orcid.org/0000-0003-0014-3354
Naoki Koshimoto https://orcid.org/0000-0003-2302-9562
Jessica R. Lu https://orcid.org/0000-0001-9611-0009
Joshua W. Blackman https://orcid.org/0000-0001-5860-1157
Clément Ranc https://orcid.org/0000-0003-2388-4534
Sean K. Terry https://orcid.org/0000-0002-5029-3257
Andrew A. Cole https://orcid.org/0000-0003-0303-3855
Akihiko Fukui https://orcid.org/0000-0002-4909-5763
```

References

```
Bachelet, E., Specht, D., Penny, M., et al. 2022, A&A, 664, A136
Batista, V., Beaulieu, J.-P., Bennett, D. P., et al. 2015, ApJ, 808, 170
Batista, V., Beaulieu, J.-P., Gould, A., et al. 2014, ApJ, 780, 54
```

```
Bennett, D. 2018, Keck Observatory Archive, N02, 124
Bennett, D. P. 2008, in Exoplanets, ed. J. Mason (Berlin: Springer)
Bennett, D. P. 2010, ApJ, 716, 1408
Bennett, D. P., Anderson, J., Beaulieu, J.-P., et al. 2010a, arXiv:1012.4486
Bennett, D. P., Anderson, J., Bond, I. A., Udalski, A., & Gould, A. 2006,
   ApJL, 647, L171
Bennett, D. P., Anderson, J., & Gaudi, B. S. 2007, ApJ, 660, 781
Bennett, D. P., Batista, V., Bond, I. A., et al. 2014, ApJ, 785, 155
Bennett, D. P., Bhattacharya, A., Anderson, J., et al. 2015, ApJ, 808, 169B
Bennett, D. P., Bhattacharya, A., Beaulieu, J.-P., et al. 2020a, AJ, 159, 68
Bennett, D. P., Rhie, S., et al. 2010b, ApJ, 713, 837
Bennett, D. P., & Rhie, S. H. 1996, ApJ, 472, 660
Bennett, D. P., Udalski, A., Bond, I. A., et al. 2018, AJ, 156, 113
Bertin, E., & Arnouts, S. 1996, A&AS, 117, 393
Bertin, E., Mellier, Y., Radovich, M., et al. 2002, The TERAPIX Pipeline, ASP
  Conference Series, 281, 228
Bhattacharya, A., Anderson, J., Beaulieu, J.-P., et al. 2019b, HST Proposal,
  15690
Bhattacharya, A., Beaulieu, J.-P., Bennett, D. P., et al. 2018, AJ, 156, 289
Bhattacharya, A., Bennett, D. P., Anderson, J., et al. 2017, AJ, 154, 2
Bhattacharya, A., Bennett, D. P., Beaulieu, J. P., et al. 2021, AJ, 162, 60B
Bhattacharya, A., Bennett, D. P., Bond, I. A., et al. 2016, AJ, 152, 140
Blackman, J. W., Beaulieu, J. P., Bennett, D. P., et al. 2021, Natur, 598,
Bond, I. A., Udalski, A., Jaroszynski, M., et al. 2004, ApJ, 606L, 155B
Boyajian, T. S., van Belle, G., & von Braun, K. 2014, AJ, 147, 47
Dang, L., Calchi Novati, S., Carey, S., et al. 2020, MNRAS, 497, 5309
Delfosse, X., Forveille, T., Ségransan, D., et al. 2000, A&A, 364, 217
Dong, S., Bond, I. A., Gould, A., et al. 2009, ApJ, 698, 1826
Dong, S., Gould, A., Udalski, A., et al. 2009, ApJ, 695, 970
Dutra, C. M., Santiago, B. X., Bica, E. L. D., & Barbuy, B. 2003, MNRAS,
Gaudi, B. S. 2012, ARA&A, 50, 411
Gaudi, B. S., Bennett, D. P., Udalski, A., et al. 2008, Sci, 319, 927
Gould, A., & Loeb, A. 1992, ApJ, 396, 104G
Gould, A., Ryu, Y.-H., Calchi Novati, S., et al. 2020, JKAS, 53, 9
Henry, T. J., Franz, O. G., Wasserman, L. H., et al. 1999, ApJ, 512, 864
Henry, T. J., & McCarthy, D. W., Jr. 1993, AJ, 106, 773
Kenyon, S. J., & Hartmann, L. 1995, ApJSS, 101, 117
Kervella, P., Thévenin, F., Di Folco, E., & Ségransan, D. 2004, A&A, 426, 297
Koshimoto, N., & Bennett, D. 2020, AJ, 159, 268
Koshimoto, N., Bennett, D. P., & Suzuki, D. 2020, AJ, 159, 268
Lissauer, J. J. 1993, ARA&A, 31, 129
Lu, J. 2022, Keck-DataReductionPipelines/KAI: v1.0.0 Release of KAI,
  Zenodo, doi:10.5281/zenodo.6522913
Lu, J. R. 2008, PhD thesis, UCLA
Minniti, D., Lucas, P. W., Emerson, J. P., et al. 2010, NewA, 15, 433
Muraki, Y., Han, C., Bennett, D. P., et al. 2011, ApJ, 741, 22
Nataf, D. M., Gould, A., Fouqué, P., et al. 2013, ApJ, 769, 88
Penny, M. T., Gaudi, B. S., Kerins, E., et al. 2019, ApJS, 241, 3P
Pollack, J. B., Hubickyj, O., Bodenheimer, P., et al. 1996, Icar, 124, 62
Quenouille, M. H. 1949, Ann. Stat., 20, 355
Quenouille, M. H. 1956, Biometrika., 43, 353
Rhie, S. H., Becker, A. C., Bennett, D. P., et al. 1999, ApJ, 522, 1037
Service, M., Lu, J. R., Campbell, R., et al. 2016, PASP, 128, 095004
Spergel, D., Gehrels, N., Baltay, C., et al. 2015, arXiv:1503.03757
Stetson, P. B. 1987, PASP, 99, 1918
Street, R. A., Udalski, A., Calchi Novati, S., et al. 2016, ApJ, 819, 93
Sumi, T., Udalski, A., Bennett, D. P., et al. 2016, ApJ, 825, 112
Szymański, M. K., Udalski, A., Soszyński, I., et al. 2011, AcA, 61, 83
Terry, S. K., Bhattacharya, A., Bennett, D. P., et al. 2021, AJ, 161, 54
Tierney, L., & Mira, A. 1999, Stat. Med., 18, 2507
Tukey, J. W. 1958, The Annals of Mathematical Statistics, 29, 614
Udalski, A., Yee, J. C., Gould, A., et al. 2015, ApJ, 799, 237
Vandorou, A., Bennett, D. P., Beaulieu, J.-P., et al. 2020, AJ, 160, 121
Wizinowich, P., Action, S., Shelton, C., et al. 2000, PASP, 112, 315
Yelda, S., Lu, J. R., Ghez, A. M., et al. 2010, ApJ, 725, 331
```